Supporting Information

Constructing Ternary Double Bulk Heterojunction Organic Solar Cells via Layer-by-Layer Deposition Method

Jie Chi[1], Tengfei Han[1], Ran Dong[1], ShuLin Han[1], Lei Cai[1], Hang Zhou[2], Jian Wang[3], Fujun Zhang[2]*, and Qianqian Sun[1]**

[1]Collaborative Innovation Center of Light Manipulations and Applications, School of Physics and Electronics, Shandong Normal University, Jinan 250014, China

[2]Key Laboratory of Luminescence and Optical Information Ministry of Education, Beijing Jiaotong University, Beijing 100044, China

[3]College of Physics and Electronic Engineering, Taishan University, Taian 271021, China

[*]Authors to whom correspondence should be addressed: wangjian@tsu.edu.cn; fjzhang@bjtu.edu.cn; and qianqiansun@sdnu.edu.cn

1. Experimental section

1.1 Device fabrication

The indium tin oxide (ITO) glass substrates were sequentially pre-cleaned in the ultrasonic baths containing detergent, deionized water, or ethanol, respectively. The cleaned ITO substrate was blown-dried with nitrogen and treated with oxygen plasma for 70 second (s) to improve work function and clearance. Subsequently, poly (3,4-ethylene dioxythiophene):poly (styrene sulfonate) (PEDOT:PSS, purchased from H.C. Starck Co. Ltd.) solution was spin-coated on ITO substrates at 5000 round per minute (rpm) for 30 s and dried at 150 ℃ for 15 minutes (min) in atmospheric air. Then ITO substrates coated with PEDOT:PSS films were transferred into a high-purity nitrogen-filled glove box. The active layer material was purchased from Solarmer Materials Inc. The specific batch numbers as follows: PM1: batch No.: QO801A; L8-BO: batch No.:DO206A; BTP-eC9: batch No.:CN312A. Both the BHJ and double-BHJ devices

were fabricated with a conventional device structure of ITO/PEDOT:PSS/active layer/PDINN/Ag. For the BHJ devices, the active layers were spin-coated from 15.4 mg ml^{-1} chloroform solution (D:A=1:1.2, PM1:L8-BO with 0.4 vol% DIO, PM1:BTP-eC9 with 0.5 vol% DIO) at 3000 rpm for 40 s. For the double-BHJ devices, the PM1:BTP-eC9 and PM1:L8-BO solutions were diluted to 6-15.4 and 9-15.4 *mg/ml*, respectively. Then, the active layers were thermally annealed at 60 ℃ for 5 min. The methanol solution of PDINN (1.5 mg ml^{-1}) was spin-coated on the active layer at 3000 rpm for 30 s. Finally, a 100 nm Ag layer was thermally deposited under the vacuum condition of 6×10^{-5} Pa. The active area was approximately 3.8 mm^2, which was defined by the overlapping area of the ITO anode and Ag cathode.

1.2 Measurements and Instruments

The contact angles of films were characterized by the Contact Angle meter. The absorption spectra of films were measured using a PERSEE TU-1900 spectrophotometer. The current density-voltage (*J-V*) curves of the OSCs were measured under 1 sun AM 1.5 G illumination (100 mW cm^{-2}) in a high-purity nitrogen-filled glove box by using a Keithley 2400 source meter. The AM 1.5 G illumination was provided by XES-50S2 (SAN-EI Electric Co., Ltd.) solar simulator (AAA class, 40 × 40 mm^2 effective irradiated area). Fourier transform photocurrent spectroscopy-external quantum efficiency (FTPS-EQE) was recorded by Fourier-transform photocurrent spectroscopy (PECT-600, Enli Technology Co., Ltd.). The external quantum efficiency (EQE) spectra of OSCs were measured by using a Zolix Solar Cell Scan 100 in atmospheric air. Electrochemical impedance spectroscopy (EIS) was measured in atmospheric air and dark conditions by an electrochemical workstation (CHI 760 E). In-situ UV-Vis absorption spectra measurements were performed by the DU-200 dynamic spectrometer in transmission mode with a time interval of 0.03 s. Grazing incidence wide angle X-ray scattering (GIWAXS) measurements were accomplished at the PLS-II 9A U-SAXS beamline of the Pohang Accelerator Laboratory in Korea. The morphology images of films were characterized by an atomic force microscope (AFM, Horiba Bruker Multimode 8). The transmission electron microscopy (TEM) images were measured using an HT7800 electron microscope. The

film-depth-dependent light absorption spectroscopy (FLAS) was acquired upon a film-depth-dependent light absorption spectrometer (PU100, Puguangweishi Co. Ltd). The transient absorption (TA) measurements were performed using a fiber laser (1030 nm, 100kHz repetition rate, 9.5 μJ/pulse, YF-FL-10-100-IR, Yacto-Technology, China) as the laser source and a femto-TA100 spectrometer (Time-Tech Spectra, China). The photoluminescence (PL) spectra of films were measured by a fluorescence spectrophotometer (FLS 1000).

1.3 Calculations and Equations

The measured contact angle values θ are input into the Wu model to calculate the polar surface energy (γ^p) and dispersive surface energy (γ^d) of films according to the following equation.

$$\gamma_W(1+cos\theta_W)=\frac{4\gamma_W^d\gamma^d}{\gamma_W^d+\gamma^d}+\frac{4\gamma_W^p\gamma^p}{\gamma_W^p+\gamma^p} \quad (1.3.1)$$

$$\gamma_{EG}(1+cos\theta_{EG})=\frac{4\gamma_W^d\gamma^d}{\gamma_W^d+\gamma^d}+\frac{4\gamma_{EG}^p\gamma^p}{\gamma_{EG}^p+\gamma^p} \quad (1.3.2)$$

$$\gamma_W=\gamma_W^d+\gamma_W^p \quad (1.3.3)$$

$$\gamma_{EG}=\gamma_{EG}^d+\gamma_{EG}^p \quad (1.3.4)$$

$$\gamma^{tot}=\gamma^d+\gamma^p \quad (1.3.5)$$

Here, W and EG refer to deionized water and ethylene glycol, θ_W and θ_{EG} are contact angle values when W and EG are the probing liquids. γ_W and γ_{EG} are surface energy values when W and EG are the probing liquids. The total surface energy γ^{tot} is equal to the sum of γ^d and γ^p.

The compatibility between two organic photovoltaic materials can be evaluated by the Flory-Huggins interaction parameter χ using the following equation.

$$\chi_{A:B}=\left(\sqrt{\gamma_A}-\sqrt{\gamma_B}\right)^2 \quad (1.3.6)$$

Where γ_A and γ_B represent the γ^{tot} of the corresponding films of materials A and B.

The lower $\chi_{A:B}$ means better compatibility between A and B.

The overall energy loss can be divided into three parts:

$$E_{loss} = \Delta E_1 + \Delta E_2 + \Delta E_3 \quad (1.3.7)$$

$$\Delta E_1 = E_g - qV_{OC}^{SQ} \quad (1.3.8)$$

$$\Delta E_2 = qV_{OC}^{SQ} - qV_{OC}^{rad} \quad (1.3.9)$$

$$\Delta E_3 = qV_{OC}^{rad} - qV_{OC} \quad (1.3.10)$$

Where E_g is the optical band gap; q is the elementary charge; $V_{OC}^{SQ}$is the maximum voltage given by the Shockley-Queisser limit; V_{OC}^{rad} is the open-circuit voltage when radiative recombination is the only recombination mechanism in the device; ΔE_1 is the energy loss of radiative recombination above the bandgap; ΔE_2 is the energy loss of radiative recombination below the bandgap; ΔE_3 is the energy loss of non-radiative recombination.

The E_g is calculated from the following equation:

$$\frac{E_g}{q} = \frac{\int_a^b E \cdot P(E) \cdot dE}{\int_a^b P(E) \cdot dE} \quad (1.3.11)$$

Here, P(E)=dEQE/dE and P(a)=P(b)=0.5×max[P(E_g)].

The $V_{OC}{}^{rad}$ is calculated from the following equation:

$$V_{OC}{}^{rad} = \frac{kT}{q} ln\left[\frac{J_{SC}}{q\int_0^\infty EQE(E)\emptyset_{BB}dE} + 1\right] \quad (1.3.12)$$

here $\emptyset_{BB}$ is the black body spectrum, given by Planck's law:

$$\emptyset_{BB}(E) = \frac{2\pi E^2}{h^3c^2\left[\exp\left(\frac{E}{kT}\right) - 1\right]} \approx \frac{2\pi E^2}{h^3c^2}\exp\left(-\frac{E}{kT}\right) \quad (1.3.13)$$

Where h is Planck's constant, and c is the light speed in the vacuum.

The Urbach rule is expressed as follows:

$$\alpha(E) = \alpha_0 e^{\frac{(E - E_0)}{E_u}} \quad (1.3.14)$$

Where $\alpha(E)$ is the absorption coefficient, α_0 is the optical absorption coefficient,

and E is the photon energy. The E_u values can be obtained by fitting the FTPS-EQE curves with the above equation. The smaller E_u represents lower energetic disorder.

The exciton dissociation efficiency (P_{diss}) and charge collection efficiency (P_{coll}) are calculated by measuring the characteristic curves of the photogenerated current density (J_{ph}) versus the effective voltage (V_{eff}). The J_{ph} is defined as $J_{ph} = J_L$-J_D, where J_L and J_D are the current density under illumination and darkness, respectively. The V_{eff} is defined as $V_{eff} = V_0$-V_{appl}, where V_0 is the voltage at which $J_{ph} = 0$ and V_{appl} is the applied voltage. At high effective voltages (greater than 2 V), the photovoltaic current density reaches saturation (J_{sat}). The exciton dissociation efficiency (P_{diss}) can be calculated from J_{ph}*/J_{sat}, where J_{ph}* is the J_{ph} under the short-circuit condition, and the charge collection efficiency (P_{coll}) can be calculated from $J_{ph}^{\#}/J_{sat}$, where $J_{ph}^{\#}$ is the J_{ph} at the maximum output power.

The carrier mobility is measured using the space-charge-limit current (SCLC) method. The structures of the hole-only and electron-only devices are ITO/PEDOT:PSS/active layer/MoO_3/Ag and ITO/ZnO/active layer/PDINN/Ag, respectively. The devices are fabricated under optimized conditions. The mobility is determined by fitting the dark current to the model of a single carrier SCLC, according to the equation:

$$J = \frac{9}{8}\varepsilon_r\varepsilon_0\mu\frac{V^2}{L^3} \tag{1.3.15}$$

Where J is the current density, d is the film thickness of the active layer, μ is the charge carrier mobility, ε_r is the relative dielectric constant of the transport medium, and ε_0 is the permittivity of free space. The ε_r parameter is assumed to be 3, which is a typical value for organic materials. In organic materials, charge mobility is usually field-dependent and can be described by the disorder formalism, typically varying with an electric field, $E = \frac{V}{L}$, according to the equation:

$$\mu = \mu_0 exp\left[0.89\gamma\sqrt{\frac{V}{L}}\right] \tag{1.3.16}$$

Where μ_0 is the charge mobility at zero electric fields and γ is a constant. Then, the Mott-Gurney equation can be described by:

$$J = \frac{9}{8}\varepsilon_r\varepsilon_0\mu_0\frac{V^2}{L^3}exp\left[0.89\gamma\sqrt{\frac{V}{L}}\right] \quad (1.3.17)$$

In this case, the charge mobilities are estimated using the following equation:

$$\ln\left(\frac{JL^3}{V^2}\right) = 0.89\gamma\sqrt{\frac{V}{L}} + \ln\left(\frac{9}{8}\varepsilon_r\varepsilon_0\mu_0\right) \quad (1.3.18)$$

The carrier mobility can be calculated from the slope of the curves.

The relationship between V_{OC} and light intensity is as follows: $V_{OC} \propto \beta(KT/q)ln(P_{light})$, where k, T, and q are Boltzmann's constant, absolute temperature, and elementary charge, respectively. When the β-value is close to 1, the bimolecular recombination dominates. When the β-value is close to 2, the trap-assisted recombination dominates. The relationship between J_{SC} and P_{light} is as follows: $J_{SC} \propto (P_{light})^{\alpha}$, with α close to 1 indicating low loss of bimolecular recombination.

To further investigate the charge transport and recombination, electrochemical impedance spectroscopy (EIS) analysis was carried out under simulated sunlight and dark conditions with V_{OC} applied bias in the range of 1 Hz and 1 MHz. The equivalent circuit during illumination consists of series resistance (R_{OS}), charge transfer resistance (R_{CT}), and a constant phase element (CPE). The R_{OS} is related to the electrode resistance and the bulk resistance of the active layer, which can be reflected by the onset of the Nyquist diagram. The R_{CT} is the sum of the interfacial resistances between the donor and acceptor and between the active layer and the electron transport layer. The charge recombination resistance (R_{REC}) in equivalent circuit depends on the non-radiative recombination of the device under dark conditions. The smaller charge transfer resistance (R_{CT}) in equivalent circuit corresponds to a smaller radius of the Nyquist curve, which represents more efficient charge transport. The charge recombination resistance (R_{REC}) in equivalent circuit depends on non-radiative recombination under dark conditions. The larger R_{REC} value represents a lower probability of charge recombination in OSCs.

The film formation process of the active layer can be divided into three distinct stages according to the variation of donor or acceptor absorption peak position: I) the

rapid solvent evaporation stage; II) the nucleation and crystallization stage; III) the dry film stage. In stage I, the donor and acceptor absorption peaks appear immediately when the solution drops onto the substrate. The peak intensities of donor and acceptor rapidly decrease as a large amount of solution spreads outward in the radial direction during spin-coating. Throughout the entire stage I, the positions of the donor and acceptor absorption peaks remain essentially unchanged due to the film being in the liquid phase at this time. In stage II, the rapid evaporation of the solvent causes the solution concentration to exceed the dissolution limit. The position of the donor and acceptor absorption peaks shows a significant red shift, which indicates nucleation and crystallization of the donor and acceptor in the blend. In stage III, the intensities and positions of the donor and acceptor peaks remain constant, which indicates that the film has been formed.

The peak location and FWHM measured from GIWAXS are entered into the following formula to calculate the d-spacing and CCL of the film.

$$d\ spacing = \frac{2\pi}{q} \tag{1.3.19}$$

$$CCL = \frac{2\pi k}{f_{whm}} \tag{1.3.20}$$

Where q is expressed as the peak location, k is the shape factor with a usual value of 0.9 and f_{whm} is the full width at the half maximum of the diffraction peak.

The fractions (f) of the active layer surface covered by acceptor are calculated by using the Cassie–Baxter equation,

$$cos\theta = f cos\theta_A - (1 - f) cos\theta_D \tag{1.3.21}$$

where θ_A, θ_D and θ are the measured *WCAs* of pure acceptor film, pure donor film and the blend films, respectively.

2. Additional experimental results

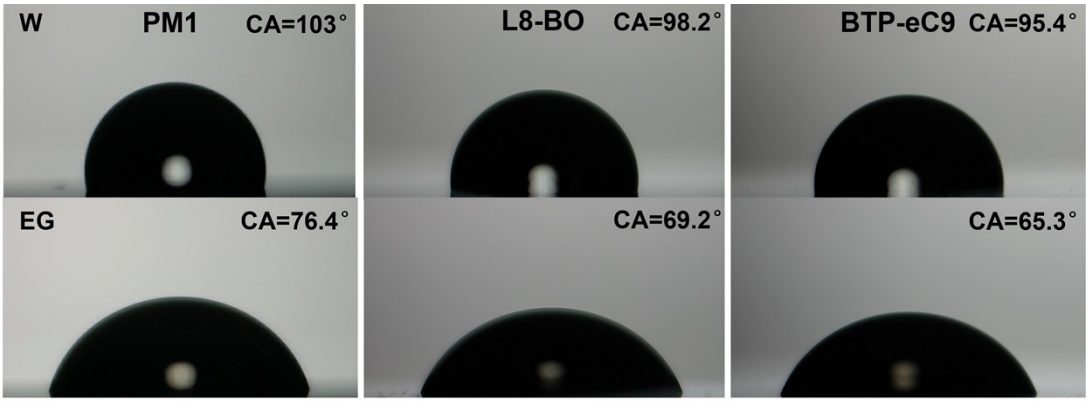

Figure S1. Contact angle images of W and EG on the pure PM1, L8-BO, and BTP-eC9 films.

Table S1. Contact angles, surface free energies for the three pure films, and χ between three materials.

Films	θ_w (°)	θ_{EG} (°)	γ^d (mN m^{-1})	γ^p (mN m^{-1})	γ^{tot} (mN m^{-1})	χ	
PM1	103	76.4	18.26	4.54	22.80	$\chi_{PM1:L8-BO}$	0.106
L8-BO	98.2	69.2	20.38	5.63	26.01	$\chi_{PM1:BTP-eC9}$	0.234
BTP-eC9	95.4	65.3	21.17	6.48	27.65	$\chi_{L8-BO:BTP-eC9}$	0.025

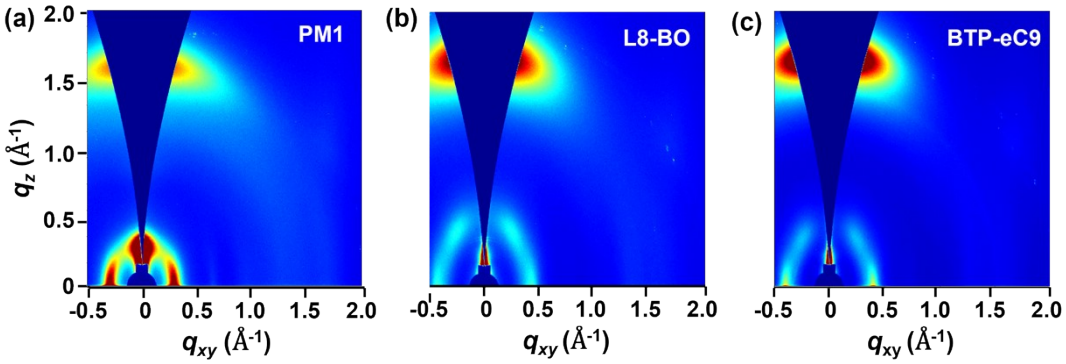

Figure S2. 2D GIWAXS images of pure PM1 (a), L8-BO (b), and BTP-eC9 (c) films.

Table S2. Related GIWAXS date of pure films.

Films	(100) peak in IP direction				(010) peak in OOP direction			
	Q (Å^{-1})	d-spacing (Å)	FWHM (Å^{-1})	CCL (Å)	Q (Å^{-1})	d-spacing (Å)	FWHM (Å^{-1})	CCL (Å)
PM1	0.29	21.68	0.109	51.65	1.66	3.79	0.279	20.28
L8-BO	0.42	14.80	0.164	34.53	1.71	3.68	0.299	18.85
BTP-eC9	0.39	16.06	0.104	54.58	1.73	3.63	0.249	22.72

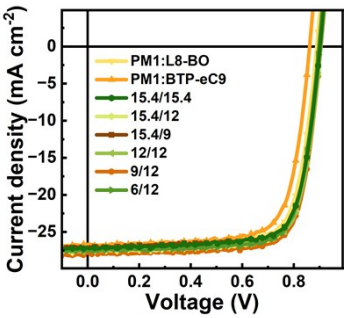

Figure S3. *J-V* curves of the BHJ and double-BHJ OSCs with different concentrations.

Table S3. Photovoltaic parameters of the BHJ and double-BHJ OSCs with different concentrations.

Active layers	Concentration [mg ml^{-1}]	V_{OC} [V]	J_{SC} [mA cm^{-2}]	$J_{SC\ cal}$ [mA cm^{-2}]	FF [%]	PCE [%]
PM1:L8-BO	15.4	0.89	26.92	26.03	75.87	18.18
PM1:BTP-eC9	15.4	0.86	26.73	25.82	74.41	17.11
PM1:BTP-eC9/ PM1:L8-BO	15.4/15.4	0.90	27.09	26.29	76.20	18.58
	15.4/12	0.91	27.48	26.53	76.41	19.10
	15.4/9	0.91	27.02	26.18	76.27	18.75
	15.4/12	0.91	27.48	26.53	76.41	19.10
	12/12	0.91	27.51	26.64	76.67	19.19
	9/12	0.91	27.80	26.98	77.57	19.62
	6/12	0.90	27.46	26.48	77.42	19.13
PM1:L8-BO/ PM1:BTP-eC9	9/12	0.87	25.94	25.02	73.35	16.55
	12/9	0.87	25.40	24.61	72.84	16.10

Table S4. Photovoltaic parameters of the double-BHJ OSCs for previous reports.

Active layers	V_{OC} [V]	J_{SC} [mA cm^{-2}]	FF [%]	PCE [%]	Reference
PDPP-3T:$PC_{71}BM$/PTB7-Th:$PC_{71}BM$	0.770	23.75	67.00	12.25	Adv. Mater. 2017, 1606729
PDPP3T:$PC_{71}BM$/FTAZ:$PC_{71}BM$	0.690	15.67	61.86	6.73	Adv. Mater. 2017, 29, 1604603
PBCB-2T:$PC_{61}BM$/PDPP2T-TT:$PC_{61}BM$	0.680	14.90	58.00	5.90	Adv. Energy Mater. 2018, 8, 1802197
PBDB-T:IT-M/PBDB-T:FOIC	0.750	24.99	63.57	11.91	Adv. Energy Mater. 2020, 10, 2000826
PTB7-Th:ITIC-Th/PBDB-T:$PC_{71}BM$	0.780	18.14	65.90	9.26	Nano Energy 74 (2020) 104883
PBDB-T: ITIC-Th/ PTB7-Th: $PC_{71}BM$	0.780	18.91	66.92	9.84	
PM6:Y6-Se-4Cl/PM6:Y6	0.840	26.30	73.00	16.40	ACS Appl. Mater. Interfaces 2021, 13, 27227−27236
PM6:Y6-Se-4Cl/PM6:IT-4Cl	0.830	27.40	68.50	15.80	
PM6:Y6/PM6:Y6	0.843	26.63	79.00	17.73	Sol. RRL 2023, 2201090
PTQ10:Y6/ PTQ10:Y6	0.855	26.70	78.00	17.81	
PM6:BTP-eC9/PM6:L8-BO	0.862	26.78	79.34	18.30	J. Phys. Chem. C 2023, 127, 19918−19926
D19-Cl:BTP-eC9/PM6:L8-BO	0.898	27.02	80.81	19.61	Adv. Mater. 2023, 35, 2208997
PM6:PY-SSe/D18-Cl:PY-Cl	0.930	26.60	78.65	19.46	Energy Environ. Sci., 2025, 18, 1812–1823

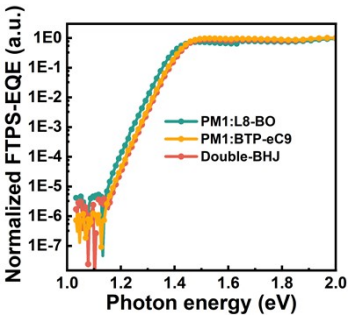

Figure S4. Normalized FTPS-EQE spectra of the BHJ and double-BHJ OSCs.

Table S5. Total, detailed energy losses and urbach energy of the BHJ and double-BHJ OSCs.

Active layers	E_g (eV)	E_{loss} (eV)	qV_{OC}^{rad} (eV)	$\Delta E_1+\Delta E_2$ (eV)	ΔE_3 (eV)	E_u (meV)
PM1:L8-BO	1.42	0.53	1.11	0.31	0.22	21.62
PM1:BTP-eC9	1.40	0.54	1.09	0.31	0.23	23.38
Double-BHJ	1.43	0.52	1.11	0.32	0.20	21.09

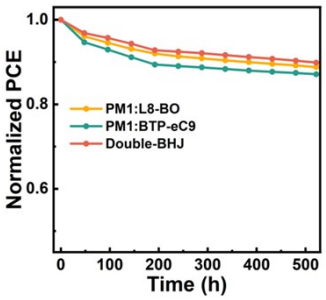

Figure S5. Decay curves of PCEs versus storage time in the N_2 environment.

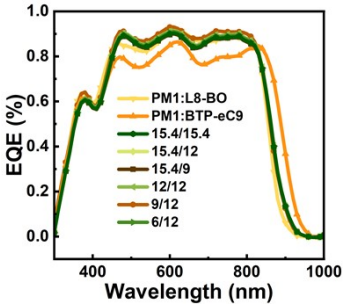

Figure S6. EQE spectra of the BHJ and double-BHJ OSCs with different concentration.

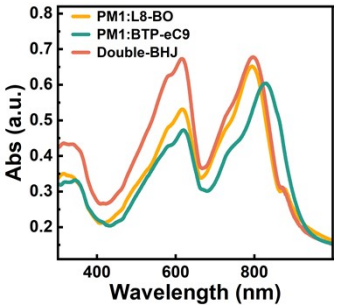

Figure S7. Absorption spectra of different blend films.

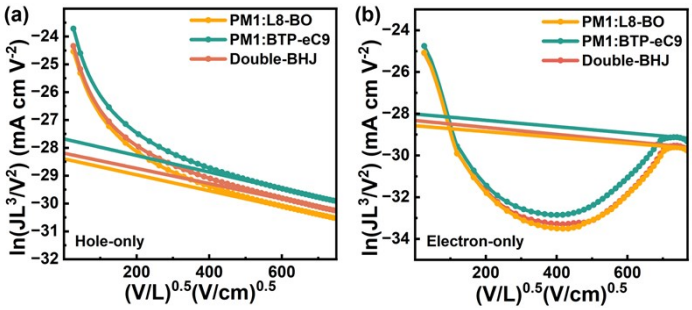

Figure S8. Ln(JL^3/V^2) versus $(V/L)^{0.5}$ curves of hole-only (a) and electron-only (b) devices.

Table S6. μ_h, μ_e, and μ_h/μ_e values of the BHJ and double-BHJ devices.

Active layers	μ_h (cm^2 V^{-1} s^{-1})	μ_e (cm^2 V^{-1} s^{-1})	μ_h/μ_e
PM1:L8-BO	1.56×10^{-3}	1.30×10^{-3}	1.20
PM1:BTP-eC9	3.18×10^{-3}	2.29×10^{-3}	1.39
Double-BHJ	1.91×10^{-3}	1.67×10^{-3}	1.12

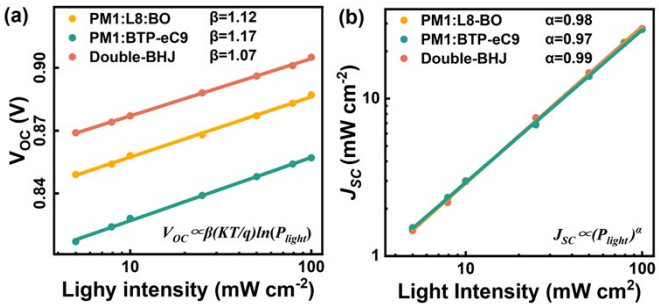

Figure S9. J_{SC} (a) and V_{OC} (b) as functions of light intensity for different devices.

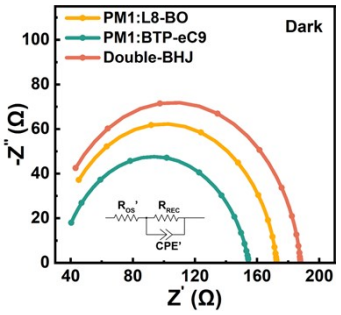

Figure S10. Nyquist plots for different devices in the dark.

Table S7. Fitted parameters of OSCs based on the BHJ and double-BHJ active layers.

Active layers	R_{OS} (Ω)	R_{CT} (Ω)	R_{REC} (Ω)
PM1:L8-BO	34.1	35.37	144.6
PM1:BTP-eC9	33.47	39.35	122.4
Double-BHJ	34.55	27.79	163.5

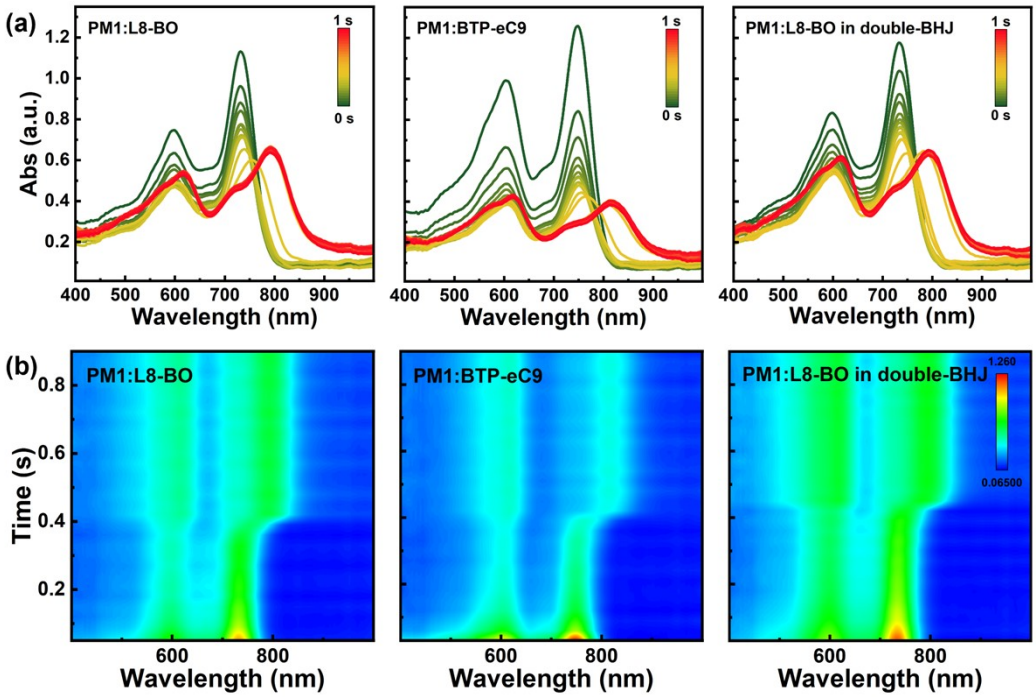

Figure S11. In-situ UV-vis absorption spectra curves (a), time-resolved UV-vis absorption spectra (b) for PM1:L8-BO, PM1: BTP-eC9, and PM1:L8-BO in double-BHJ.

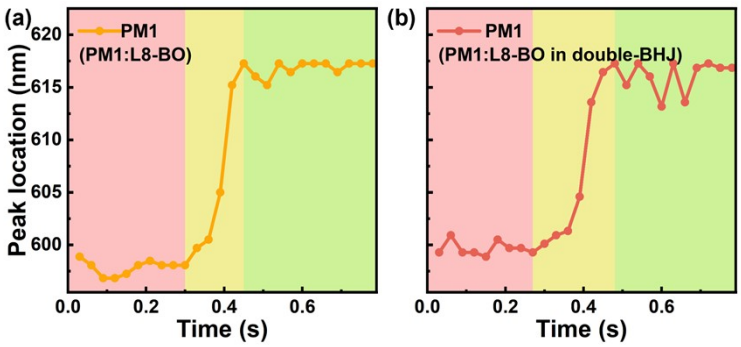

Figure S12. Time evolution of the PM1 peak position for PM1:L8-BO (a) and PM1:L8-BO in double-BHJ (b).

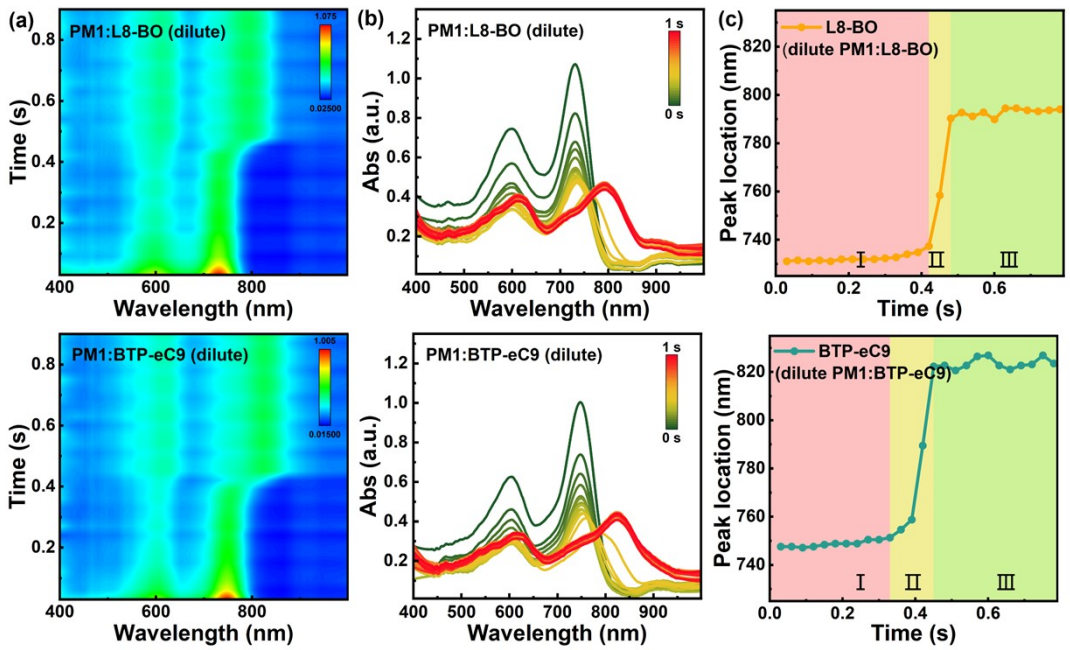

Figure S13. In-situ UV-vis absorption spectra contour maps (a), curves (b), and time evolution of acceptor peak position (c) for dilute PM1:L8-BO and dilute PM1:BTP-eC9 with the same concentration.

Table S8. Related GIWAXS data for blend films.

Films	(100) peak in IP direction				(010) peak in OOP direction			
	Q ($Å^{-1}$)	d-spacing (Å)	FWHM ($Å^{-1}$)	CCL (Å)	Q ($Å^{-1}$)	d-spacing (Å)	FWHM ($Å^{-1}$)	CCL (Å)
PM1:L8-BO	0.3	20.73	0.098	57.68	1.71	3.67	0.264	21.39
PM1:BTP-eC9	0.3	20.73	0.084	67.20	1.72	3.65	0.259	21.82
Double-BHJ	0.3	20.73	0.087	65.08	1.71	3.67	0.262	21.61

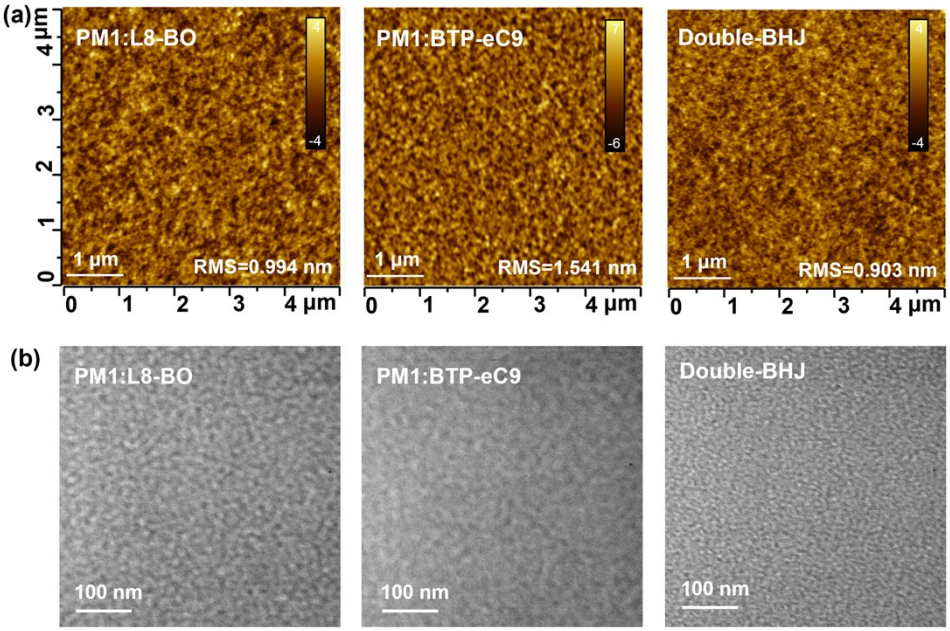

Figure S14. AFM height images (a) and TEM images (b) for different blend films.

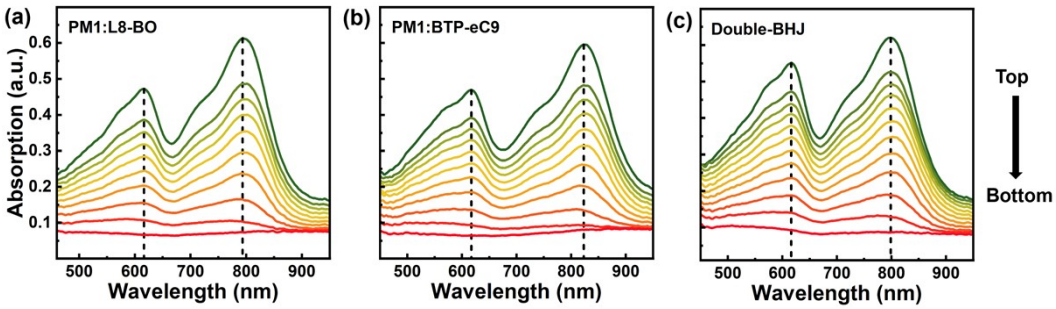

Figure S15. FLAS of PM1:L8-BO (a), PM1: BTP-eC9 (b), and double-BHJ (c) blend films.

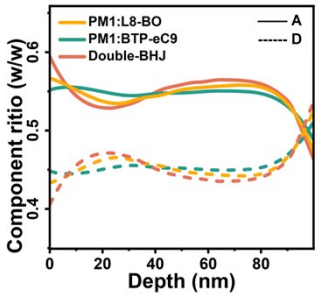

Figure S16. Composition ratio across the vertical direction of different films.

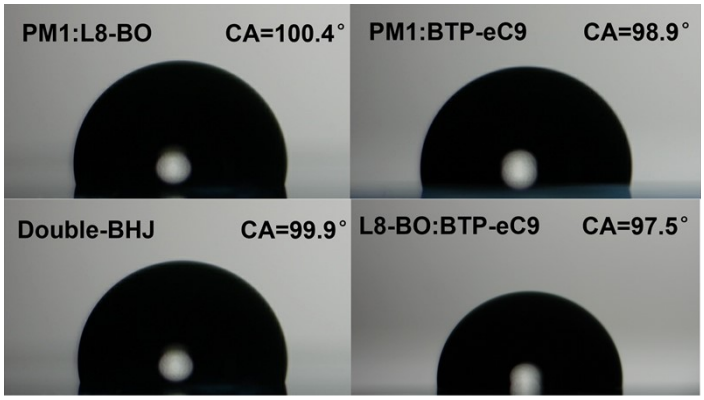

Figure S17. Water contact angle images of water on the blend films.

Table S9. θ_w, $cos\theta$ and f of the different blend films.

Films	θ_w (°)	cosθ	f (%)
PM1:L8-BO	100.4	-0.181	54.9
PM1:BTP-eC9	98.9	-0.155	53.4
Double-BHJ	99.9	-0.172	56.4

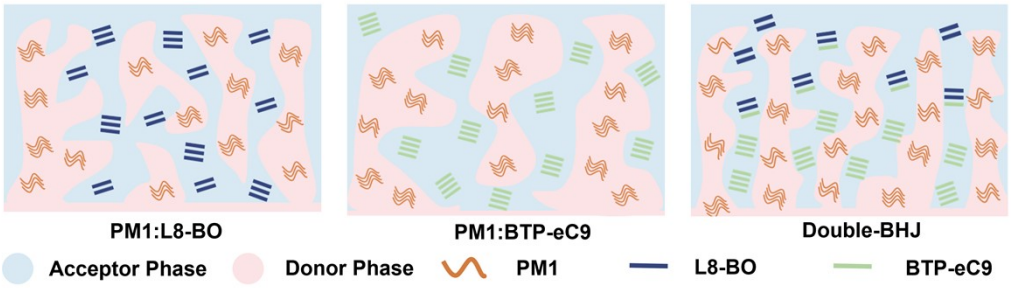

Figure S18. Schematics of components distribution and crystal situation.

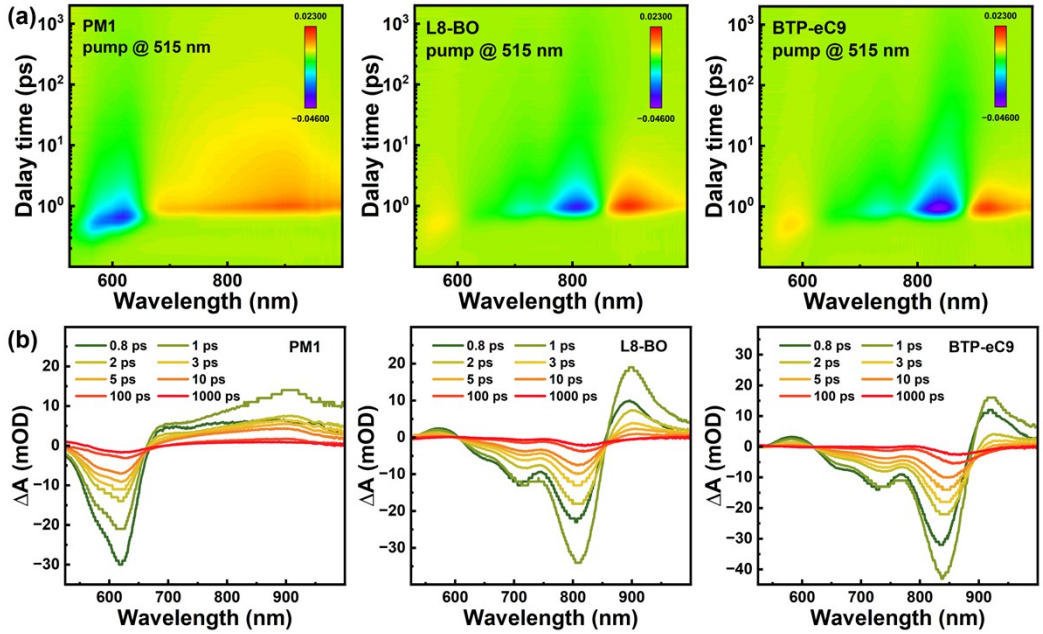

Figure S19. 2D color plots of TA spectra (a) and the extracted TA spectra (b) of the pure PM1, L8-BO, and BTP-eC9 films.

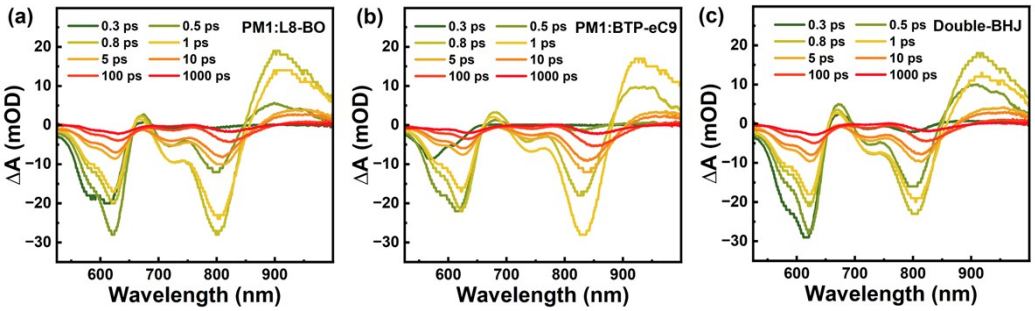

Figure S20. TA spectra of the PM1:L8-BO (a), PM1: BTP-eC9 (b), and double-BHJ (c) blend films.

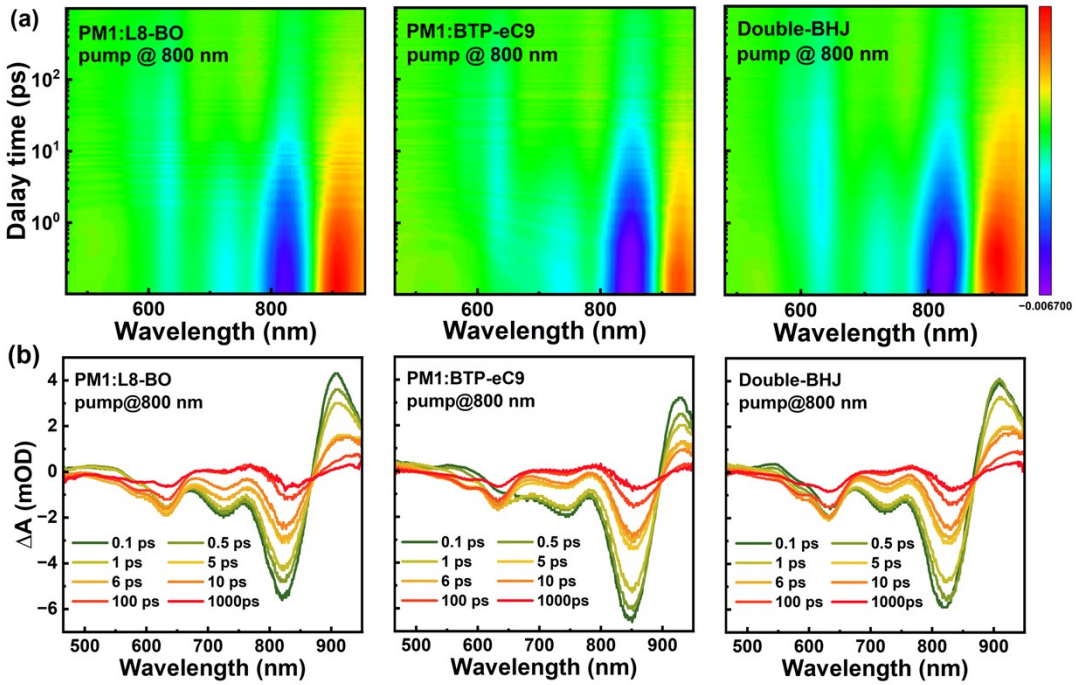

Figure S21.Fs-TAS contour maps (a) and curves (b) of different films under 800 nm pump light.

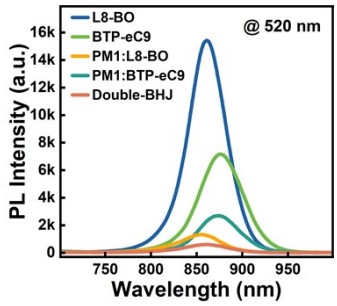

Figure S22. PL spectrum of pure acceptor films and blend films.